
CMS Physics Analysis Summary

Contact: cms-pag-conveners-susy@cern.ch

2016/08/04

Search for new physics in the all-hadronic final state with the M_{T2} variable

The CMS Collaboration

Abstract

A search for new physics is performed using events with jets and the M_{T2} variable, which is a measure of the transverse momentum imbalance in an event. The results are based on the same kinematic variable as a search with the 2015 dataset, here with a sample of proton-proton collisions collected in 2016 at a center-of-mass energy of 13 TeV with the CMS detector and corresponding to an integrated luminosity of 12.9 fb⁻¹. No excess above the standard model background is observed. The results are interpreted as limits on the masses of potential new colored particles in a variety of simplified models of supersymmetry.

1 Introduction

We present the result of a search for new physics in events with jets and significant transverse momentum imbalance. Such searches were previously conducted by both the ATLAS [1–4] and CMS [5–8] collaborations using datasets of 13 TeV proton-proton (pp) collisions. This search is a continuation of previous work [5], updated using a dataset corresponding to an integrated luminosity of 12.9 fb^{-1} of pp collisions collected during 2016 at a center-of-mass energy of 13 TeV with the Compact Muon Solenoid (CMS) detector at the LHC. We observe no evidence for an excess above the expected background from SM processes and interpret the results as limits on the production of pairs of gluinos and squarks using simplified models of supersymmetry.

2 Event selection

This search is based on similar objects and calibrations as the one performed on the 2015 dataset [5], and makes use of Monte Carlo samples produced with the same generator and simulation programs and processed with the same chain of reconstruction programs used for collision data. In the interest of brevity, we here provide only a short summary of the analysis, highlighting any changes made with respect to the earlier version of the analysis.

We select events with at least one jet and veto events with an isolated lepton or charged particle-flow candidate. Collision events are selected using triggers with varied requirements on H_T , E_T^{miss} , and H_T^{miss} . To suppress the background from SM multi-jet production, we require a transverse mass (M_{T2}) [9] of at least 200 GeV in events with at least two jets. To further protect against jet mis-measurement, we require that the minimum difference $\Delta\phi_{\text{min}}$ in azimuthal angle between the \vec{E}_T^{miss} vector and each of the leading four jets is greater than 0.3 radians.

Events with two or more jets are classified by the number of jets (N_j), the number of b-tagged jets (N_b), and the scalar sum of jet transverse momenta (H_T). Each such bin is referred to as a *topological region*. Signal regions are defined by further dividing in bins of M_{T2} . The choice of binning is identical to that used in the 2015 analysis, with the exception that the topological regions

- $H_T > 1500 \text{ GeV}, 2\text{--}6j, \geq 3b$
- $H_T > 1500 \text{ GeV}, \geq 7j, \geq 3b$,

which previously had a single M_{T2} bin, have been split into two bins: $[200, 400]$, $[400, \infty]$. Events with only one jet require that the p_T of the jet is at least 200 GeV, and are then classified according to the transverse momentum of this jet and whether the event contains a b-tagged jet, with the same choice of bins as the 2015 search.

3 Backgrounds

A jets plus E_T^{miss} final state is populated by three categories of SM processes:

- “lost lepton”, i.e. events with a lepton from a W decay where the lepton is either out of acceptance, not reconstructed, not identified, or not isolated. This background comes from both W +jets and $t\bar{t}$ +jets events.
- “irreducible”, i.e. Z +jets events where the Z boson decays to neutrinos. This background is most similar to potential signals. It is a major background in nearly all search regions, its importance decreasing with the N_b requirement.
- “instrumental background”, i.e. mostly QCD multi-jet events with no real E_T^{miss} .

These events enter a search region due to either significant jet momentum over-measurement, under-measurement, or sources of anomalous noise.

As the methods used to estimate the backgrounds are unchanged from the search performed on the 2015 dataset, only a brief summary follows.

3.1 Estimation of the background from leptonic W boson decays

Events with exactly one lepton candidate are selected using the same triggers as for signal regions and the full baseline selections are applied with the exception of the lepton veto. Selected events are binned in the H_T , N_j , and N_b dimensions but not in M_{T2} to preserve more data in each separate control region. For events with $N_j = 1$, a control region is defined for each bin of jet p_T .

The background in each signal bin is obtained using transfer factors according to:

$$N_{1\ell}^{\text{SR}}(M_{T2}) = N_{1\ell}^{\text{CR}}(H_T, N_j, N_b) \times R_{\text{MC}}^{0\ell/1\ell}(H_T, N_j, N_b) \times k_{\text{MC}}(M_{T2}) \quad (1)$$

The factor $R_{\text{MC}}^{0\ell/1\ell}(H_T, N_j, N_b)$ accounts for lepton acceptance and efficiency and the expected contribution from the decay of W bosons to hadrons through an intermediate τ lepton. It is obtained from MC and corrected for measured differences between data and simulation. The fraction of events in each topological region expected to populate a particular M_{T2} bin, $k_{\text{MC}}(M_{T2})$, is used to obtain the estimate in each search bin. The MC modeling of M_{T2} is checked in data using large-sized control samples enriched in events originating from either W +jets or $t\bar{t}$ +jets as shown in the left and right panels of Figure 1, respectively.

Uncertainties from the limited size of the control sample and from variations of all relevant theoretical and experimental quantities are evaluated and propagated to the final estimate. The dominant uncertainty on the factor $R_{\text{MC}}^{0\ell/1\ell}(H_T, N_j, N_b)$ arises from the modeling of the lepton efficiency and jet energy scale (JES) and is of order 15–20%. The uncertainty on the M_{T2} extrapolation, as large as 40%, comes primarily from the JES, the relative composition of W +jets and $t\bar{t}$ +jets, and variations of the renormalization and factorization scales. These and other uncertainties are similar to those seen previously in [5].

3.2 Estimation of the background from $Z(\nu\bar{\nu})$ +jets

The $Z \rightarrow \nu\bar{\nu}$ background is obtained from a γ +jets control sample selected using a single photon trigger, and the full baseline selection requirements are made based on kinematic variables re-calculated after removing the photon from the event to replicate the $Z \rightarrow \nu\bar{\nu}$ kinematics. Adopting a similar strategy as that used for the estimate of the lost lepton background, selected events are then binned in the H_T , N_j , and N_b dimensions but not in M_{T2} to preserve more data in each separate control region. For events with $N_j = 1$, one control region is defined for each bin of jet p_T .

The background in each signal bin is obtained using transfer factors according to:

$$N_{Z \rightarrow \nu\bar{\nu}}^{\text{SR}}(M_{T2}) = N_{\gamma}^{\text{CR}}(H_T, N_j, N_b) \times P_{\gamma} \times f \times R_{\text{MC}}^{Z/\gamma}(H_T, N_j, N_b) \times k_{\text{MC}}(M_{T2}) \quad (2)$$

A prompt photon purity (P_{γ}) of 90–100% is measured in data by performing a template fit of the charged hadron isolation distribution for each topological region. The signal shape is obtained from data by measuring the charged hadron isolation in random cones well-separated from the photon and any jets. The background shape also comes from data using a sideband in $\sigma_{i\eta j\eta}$ [10].

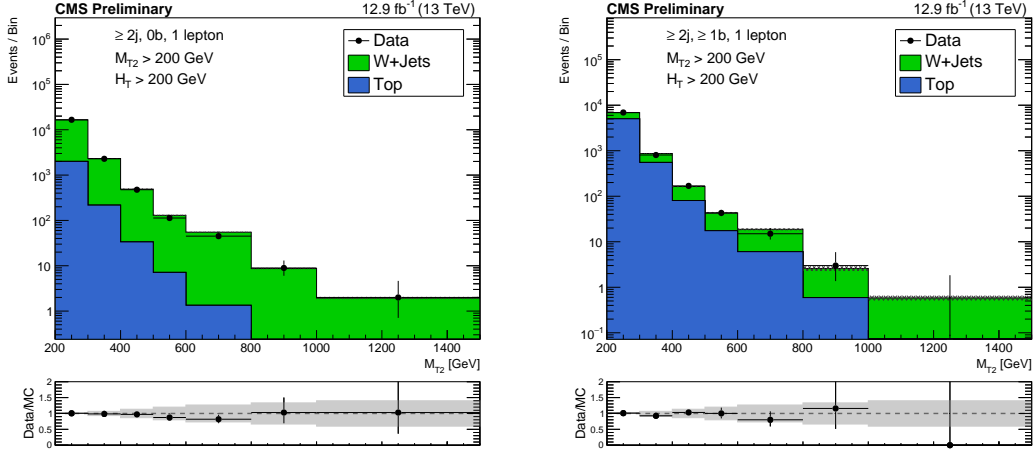


Figure 1: Shape comparison between simulation and data for the M_{T2} observable, after the simulation has been normalized to data in each of the control region bins. The left and right panels correspond to $W+\text{jets}$ and $t\bar{t}+\text{jets}$ enriched control samples, respectively.

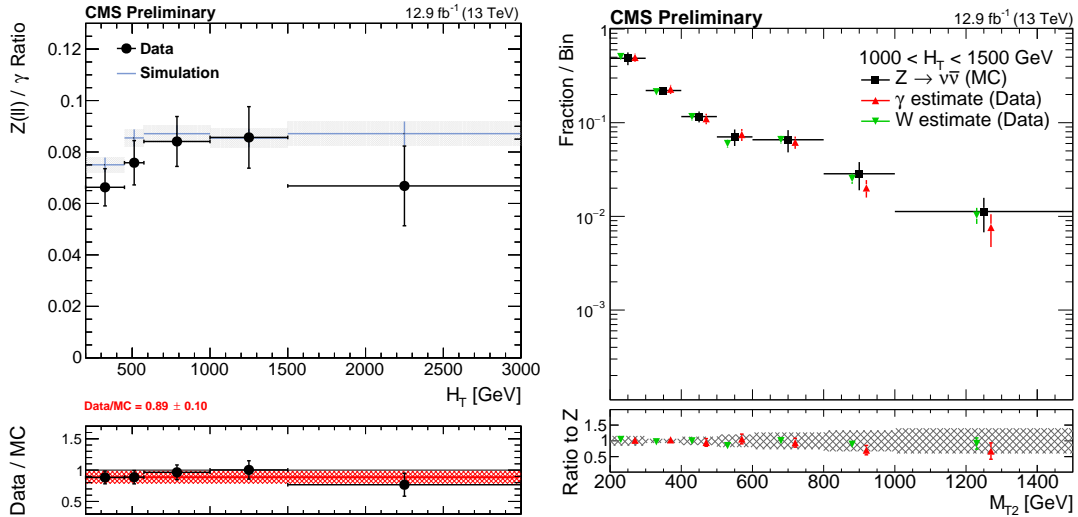


Figure 2: (Left) Ratio $R^{Z \rightarrow \ell\ell/\gamma}$ in simulation and data as a function of H_T , and the corresponding double ratio (bottom panel). The red line and uncertainty corresponds to the overall correction of 0.89 ± 0.10 as measured inclusively. (Right) The shape of the M_{T2} distribution from $Z \rightarrow \nu\bar{\nu}$ simulation compared to shapes from γ and W data control samples in the high H_T region.

An estimate of the $Z \rightarrow \nu\bar{\nu}$ background in each topological region is obtained from the corresponding photon control region yield via the factor $R_{MC}^{Z/\gamma}$, which accounts for the photon acceptance and efficiency and the relative cross sections for the production of $Z+\text{jets}$ and $\gamma+\text{jets}$ events. The ratio $R_{MC}^{Z/\gamma}$ is obtained from simulation and validated in data using $Z \rightarrow \ell^+\ell^-$ events. The left panel of Figure 2 shows the double ratio, $R_{\text{data}}^{Z \rightarrow \ell\ell/\gamma} / R_{MC}^{Z \rightarrow \ell\ell/\gamma}$, in bins of H_T . The double ratio shows no significant trend and a correction factor of 0.89 is applied to $R_{MC}^{Z/\gamma}$ to account for the observed deviation from unity.

The ratio $R_{MC}^{Z/\gamma}$ is obtained from $\gamma+\text{jet}$ events generated with Madgraph with an implicit requirement $\Delta R > 0.4$ between the prompt photon and the nearest parton. As no such require-

ment can be made in data, a correction factor $f = 0.92$ as determined from studies with Madgraph+Pythia and Pythia QCD samples is applied to account for the fraction of selected photons passing the ΔR requirement.

The fraction of events in each topological region expected to populate a particular M_{T2} bin, $k_{MC}(M_{T2})$, is used to obtain the estimate in each search bin. The MC modeling of M_{T2} is checked in data using large-sized control samples of γ +jets and $W \rightarrow \ell\nu$ events. The right panel of Figure 2 shows good agreement between the M_{T2} distribution obtained from γ and W data control samples with that from $Z \rightarrow \nu\bar{\nu}$ MC in the high H_T regions. In this comparison, the γ sample is corrected based on P_γ , f and $R_{MC}^{Z/\gamma}$, while the W sample is corrected for top contamination and $R_{MC}^{Z/W}$.

Uncertainties from the limited size of the control sample and from variations of the template fit and of all relevant theoretical and experimental quantities are evaluated and propagated to the final estimate. The dominant uncertainty on the factor $R_{MC}^{Z/\gamma}$ comes from the validation of the ratio from MC using $Z \rightarrow \ell^+\ell^-$ events, and varies between 10–100%, depending on the search region. The uncertainty on the M_{T2} extrapolation comes primarily from the JES and variations of the renormalization and factorization scales and can be as large as 40%. These and other uncertainties are similar to those seen previously in [5].

3.3 Estimation of the multi-jet background

For events with at least two jets, a multi-jet enriched control region is obtained in each H_T bin by inverting the $\Delta\phi_{\min}$ requirement described in Section 2. Events are selected using pure H_T triggers and the extrapolation from low to high $\Delta\phi_{\min}$ is based on the following ratio:

$$r_\phi(M_{T2}) = N(\Delta\phi_{\min} > 0.3) / N(\Delta\phi_{\min} < 0.3). \quad (3)$$

The ratio can be described by a power law, $a \cdot M_{T2}^b$, and the parameters a, b are determined separately in each H_T bin by fitting r_ϕ in an M_{T2} sideband in data after subtracting non-QCD contributions using simulation. An example in the high H_T region is shown in Figure 3 (left).

The inclusive multi-jet contribution in each signal region, $N_{j,b}^{SR}(M_{T2})$, is estimated using the ratio $r_\phi(M_{T2})$ measured in the M_{T2} sideband and the number of events in the low $\Delta\phi_{\min}$ control region, $N_{inc}^{CR}(M_{T2})$ according to:

$$N_{inc}^{SR}(M_{T2}) = N_{inc}^{CR} \cdot r_\phi(M_{T2}) \cdot f_j(H_T) \cdot r_b(N_j), \quad (4)$$

where f_j is the fraction of QCD events falling in bin N_j , and r_b is the fraction of events in bin N_j that fall in bin N_b . The values of f_j, r_b are measured using events with M_{T2} between 100–200 GeV in the low $\Delta\phi_{\min}$ sideband, where f_j is measured separately in each H_T bin while r_b is measured in bins of N_j , integrated over H_T , as r_b is found to be independent of the latter. Values of f_j, r_b measured in data are shown in Figure 3 (center, right) compared to simulation. Uncertainties from the limited size of the control sample and from variations of the fit and the sample composition range are evaluated and found to be of similar size as in [5], varying between 40–180%, depending on the search region.

An estimate based on $r_\phi(M_{T2})$ is not viable in the mono-jet search region so a different strategy is employed. A control region is obtained by asking for a second jet with $30 < p_T < 60$ GeV and inverting the $\Delta\phi_{\min}$ requirement. After subtracting non-QCD contributions using simulation,

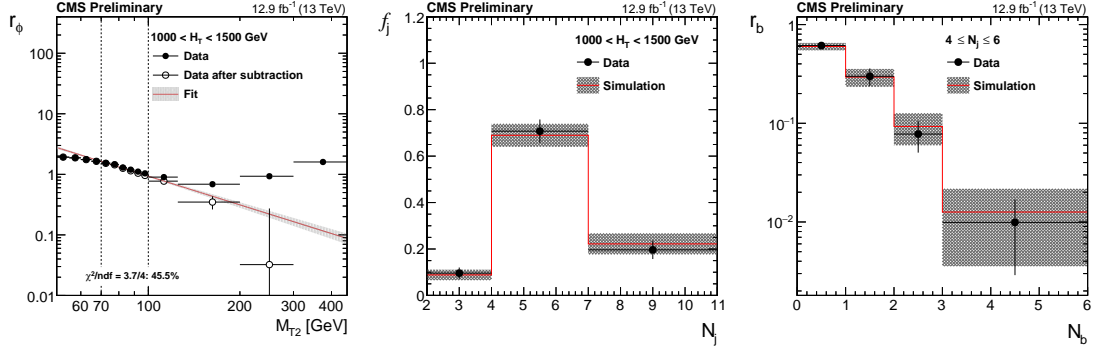


Figure 3: Distribution of the ratio r_ϕ as a function of M_{T2} for the high H_T region (left). The fit is performed to the hollow, background-subtracted data points. The full points represent the data before subtracting non-QCD backgrounds using simulation. Data point uncertainties are statistical only. The red line and the band around it show the fit to a power-law function performed in the window $70 < M_{T2} < 100$ GeV and the associated fit uncertainty. Values of f_j (center) and r_b (right) measured in data after requiring $\Delta\phi_{\min} < 0.3$ radians and $100 < M_{T2} < 200$ GeV. The bands represent both statistical and systematic uncertainties.

the data yield in the control region is taken as an estimate of the background in the mono-jet search regions. Closure tests in MC indicate a small over-estimation with the multi-jet background not expected to exceed 8% in any mono-jet search region. In all bins, a 50% systematic uncertainty is combined with the data yield in the trailing jet p_T sideband.

4 Results

A summary of the results of this search is shown in Figure 4. No significant deviations are observed from standard model expectations. Each bin in the upper panel corresponds to a single H_T , N_j , N_b search region integrated over M_{T2} . The lower panel further breaks down the background estimates and observed data yields into M_{T2} bins for the medium H_T region. The background estimates and corresponding uncertainties shown in these plots rely exclusively on the inputs from control samples and simulation as described in Section 3 and are indicated in the rest of the text as “pre-fit background” results.

We also estimate the backgrounds in the signal regions performing a maximum-likelihood fit to the data in the signal regions themselves. These fits are carried out under either the background-only or background+signal hypotheses. The estimates from the fits, which still depend on the modeling of the backgrounds from the pre-fit procedure, are indicated as “post-fit” results and are utilized to constrain models of new physics as described below. Similar comparisons between data and background predictions, for both pre- and post-fit estimates, are shown for all the remaining H_T regions in Appendix A.

4.1 Interpretation

The results of the search may be used to constrain specific models of new physics such as those shown in Figure 5.

For a given signal scenario, limits are derived by combining search regions using a modified frequentist approach [11–14]. Typical values of the uncertainties considered on the signal yield are listed in Table 1. The sources of uncertainties considered and the methods used to evaluate their effect on the interpretation are the same as those in [5]. Uncertainties due to the lumi-

osity, “ISR” recoil [15], and b-tagging and lepton efficiencies are treated as correlated across search bins. Remaining uncertainties are taken as uncorrelated.

Figure 6 shows the exclusion limits at 95% confidence level for gluino mediated bottom-squark, top-squark production, and light-flavor squark production. Exclusion limits at 95% confidence level for the direct production of bottom, top, and light-flavor squark pairs is shown in Figure 7. Table 2 summarizes the limits of the supersymmetric particles excluded in the simplified model scenarios considered. To facilitate reinterpretation of our results in the context of other models, we have also provided predictions and results in aggregated regions, made from summing up our individual signal bins in topologically similar regions. These results are presented in Appendix B.

Table 1: Typical values of the signal systematic uncertainties as evaluated for the simplified signal model of gluino mediated bottom squark production, $pp \rightarrow \tilde{g}\tilde{g}, \tilde{g} \rightarrow b\bar{b}\tilde{\chi}_1^0$. Uncertainties evaluated on other signal models are consistent with these ranges of values.

Source	Typical Values
Luminosity	6.2%
Limited size of MC samples	1–100%
Renormalization and factorization scales	5%
“ISR” recoil	0–30%
B-tagging efficiency, heavy flavor	0–40%
B-tagging efficiency, light flavor	0–20%
Lepton efficiency	0–20%
Jet energy scale	5%
Fast simulation E_T^{miss} systematic	0–5%

Table 2: Summary of 95% CL observed exclusion limits for different SUSY simplified model scenarios. The limit on the mass of the produced sparticle is quoted for a massless LSP, while for the lightest neutralino the best limit on its mass is quoted.

Simplified model	Limit on produced sparticle mass [GeV] for $m_{\tilde{\chi}_1^0} = 0$ GeV	Best limit on LSP mass [GeV]
Direct squark production		
Bottom squark	1025	425
Top squark	900	420
Single light squark	975	200
8 degenerate light squarks	1400	650
Gluino mediated production		
$\tilde{g} \rightarrow b\bar{b}\tilde{\chi}_1^0$	1750	1200
$\tilde{g} \rightarrow t\bar{t}\tilde{\chi}_1^0$	1700	1000
$\tilde{g} \rightarrow q\bar{q}\tilde{\chi}_1^0$	1650	900

5 Summary

This note presents the result of a search for new physics using events with jets and the M_{T2} variable. Results are based on a 12.9 fb^{-1} data sample of proton-proton collisions at $\sqrt{s} = 13 \text{ TeV}$ collected in 2016 with the CMS detector. No significant deviations from the standard model expectations are observed. The results are interpreted as limits on the production of new, massive colored particles. We probe gluino masses up to 1750 GeV and LSP masses up to 1200 GeV. Additional interpretations in the context of the pair production of light flavor, bottom,

and top squarks are performed, probing masses up to 1400, 1025, and 900 GeV, respectively, and LSP masses up to 650, 425, and 420 GeV in each scenario.

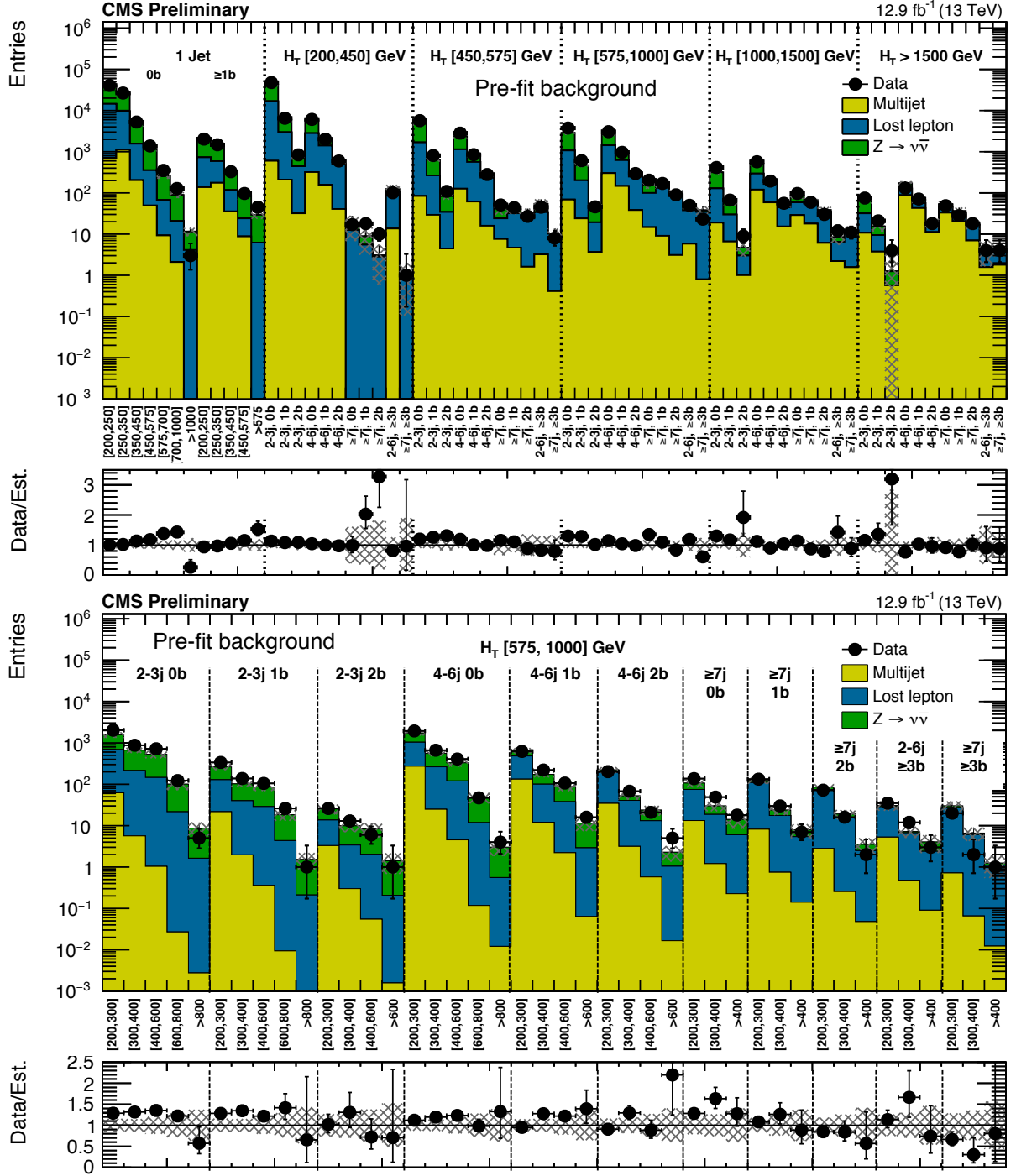


Figure 4: (Above) Comparison of estimated (pre-fit) background and observed data events in each topological region. Hatched bands represent the full uncertainty on the background estimate. The results shown for $N_j = 1$ correspond to the monojet search regions binned in jet p_T , whereas for the multijet signal regions, the notations j, b indicate N_j, N_b labeling. (Below) Same for individual M_{T2} signal bins in the medium H_T region. On the x -axis, the M_{T2} binning is shown (in GeV). Bins with no entry for data have an observed count of 0.

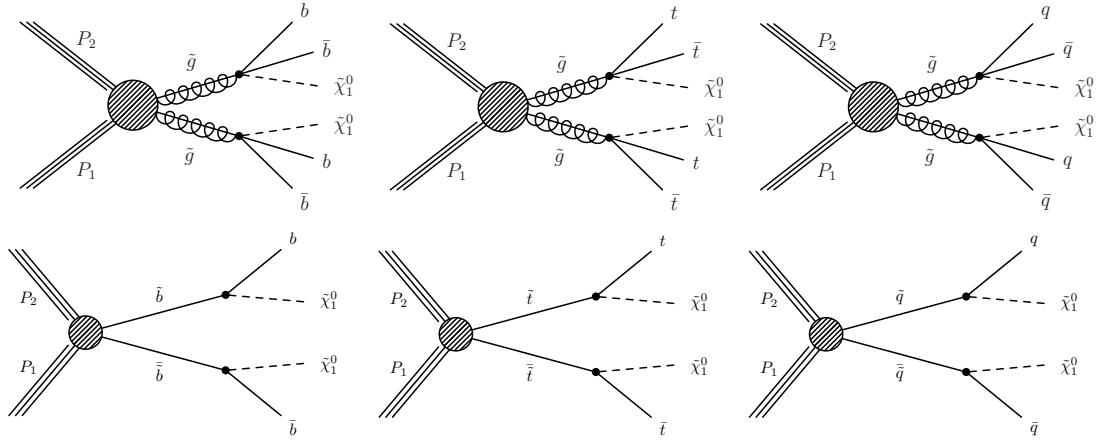


Figure 5: (Top) Diagrams for the three scenarios of gluino mediated bottom squark, top squark and light flavor squark production considered. (Bottom) Similar diagrams for the direct production of bottom, top and light flavor squark pairs.

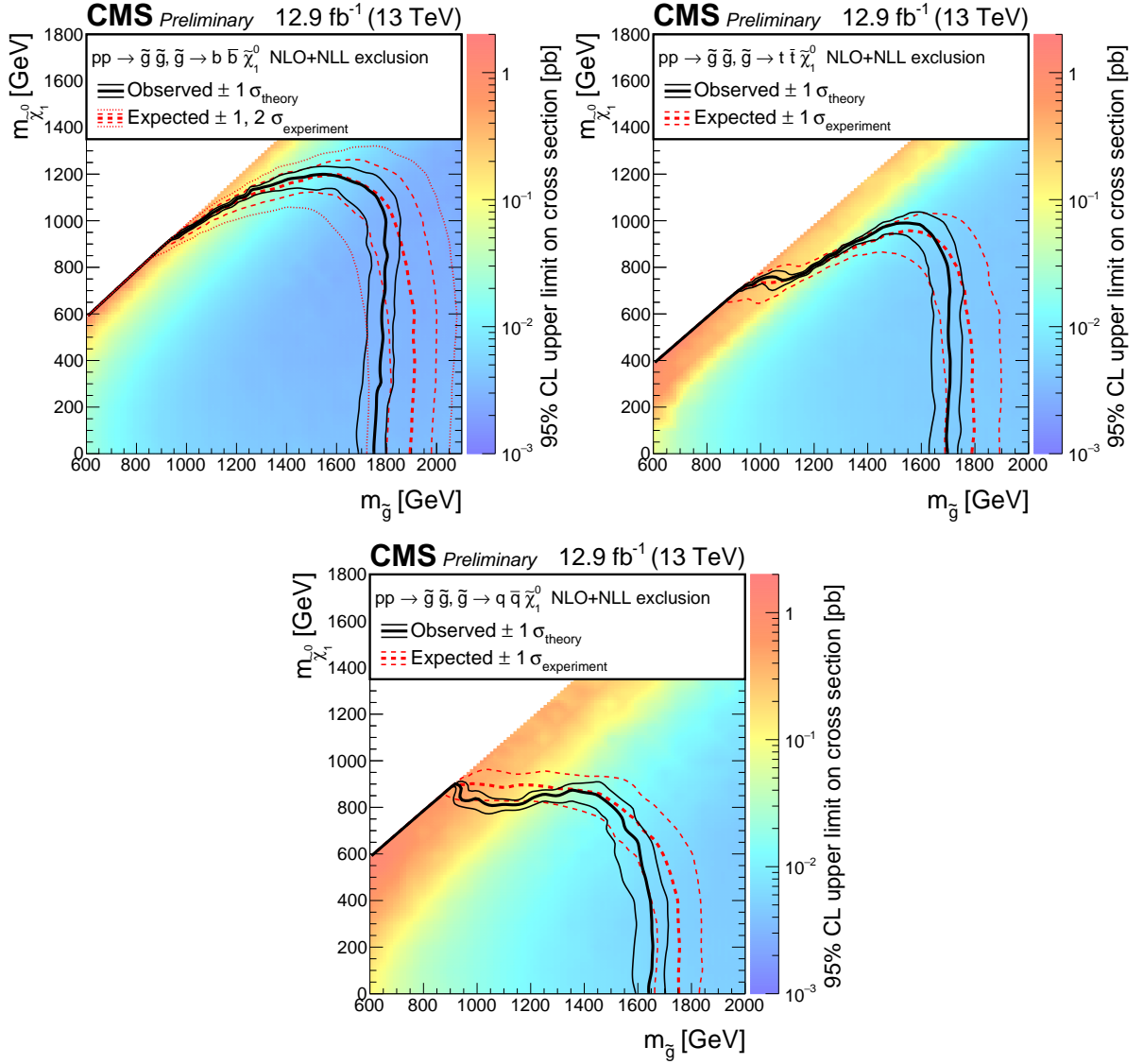


Figure 6: Exclusion limits at 95% CL on the cross sections for gluino-mediated bottom squark production (above left), gluino-mediated top squark production (above right), and gluino-mediated light-flavor squark production (below). The area to the left of and below the thick black curve represents the observed exclusion region, while the dashed red lines indicate the expected limits and their $\pm 1 \sigma_{\text{experiment}}$ standard deviation uncertainties. For the squark-pair production plot, the ± 2 standard deviation uncertainties are also shown. The thin black lines show the effect of the theoretical uncertainties σ_{theory} on the signal cross section.

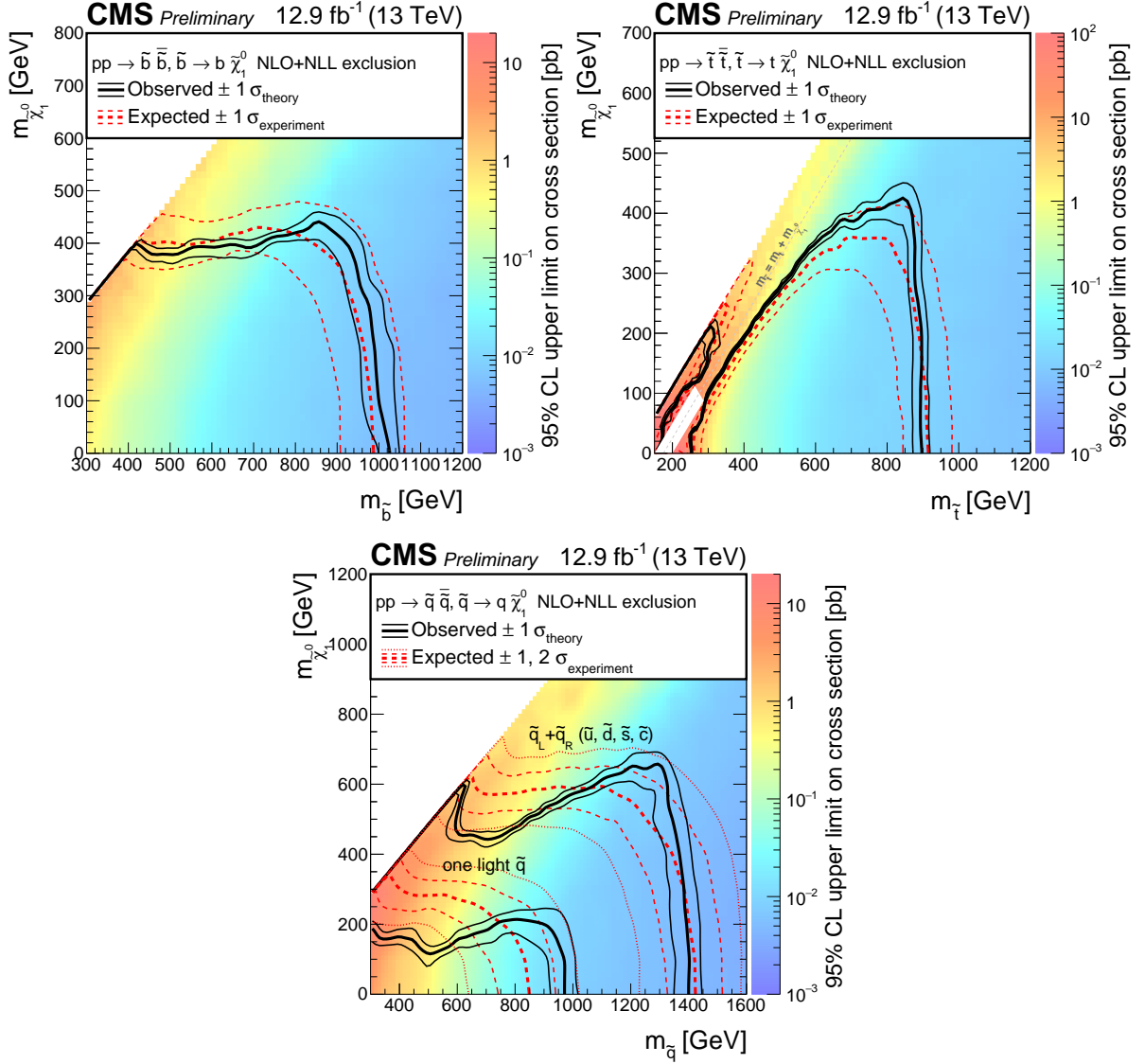


Figure 7: Exclusion limit at 95% CL on the cross sections for bottom squark pair production (above left), top squark pair production (above right), and light-flavor squark pair production (below). The area to the left of and below the thick black curve represents the observed exclusion region, while the dashed red lines indicate the expected limits and their $\pm 1\sigma_{\text{experiment}}$ standard deviation uncertainties. The thin black lines show the effect of the theoretical uncertainties σ_{theory} on the signal cross section. The white diagonal band in the upper right plot corresponds to the region $|m_{\tilde{t}} - m_t - m_{\tilde{\chi}_1^0}| < 25 \text{ GeV}$, and small $m_{\tilde{\chi}_1^0}$. Here the efficiency of the selection is a strong function of $m_{\tilde{t}} - m_{\tilde{\chi}_1^0}$, and as a result the precise determination of the cross section upper limit is uncertain because of the finite granularity of the available MC samples in this region of the $(m_{\tilde{t}}, m_{\tilde{\chi}_1^0})$ plane.

References

- [1] ATLAS Collaboration, “Search for new phenomena in final states with large jet multiplicities and missing transverse momentum with ATLAS using $\sqrt{s} = 13$ TeV proton-proton collisions”, *Phys. Lett. B* **757** (2016) 334–355, doi:10.1016/j.physletb.2016.04.005, arXiv:1602.06194.
- [2] ATLAS Collaboration, “Search for new phenomena in final states with an energetic jet and large missing transverse momentum in pp collisions at $\sqrt{s} = 13$ TeV using the ATLAS detector”, arXiv:1604.07773.
- [3] ATLAS Collaboration, “Search for squarks and gluinos in final states with jets and missing transverse momentum at $\sqrt{s} = 13$ TeV with the ATLAS detector”, arXiv:1605.03814.
- [4] ATLAS Collaboration, “Search for pair production of gluinos decaying via stop and sbottom in events with b -jets and large missing transverse momentum in pp collisions at $\sqrt{s} = 13$ TeV with the ATLAS detector”, arXiv:1605.09318.
- [5] CMS Collaboration, “Search for new physics with the MT2 variable in all-jets final states produced in pp collisions at $\sqrt{s} = 13$ TeV”, arXiv:1603.04053.
- [6] CMS Collaboration, “Search for supersymmetry in the multijet and missing transverse momentum final state in pp collisions at 13 TeV”, *Phys. Lett. B* **758** (2016) 152–180, doi:10.1016/j.physletb.2016.05.002, arXiv:1602.06581.
- [7] CMS Collaboration, “Inclusive search for supersymmetry using the razor variables at $\sqrt{s} = 13$ TeV”, Technical Report CMS-PAS-SUS-15-004, CERN, Geneva, 2015.
- [8] CMS Collaboration, “Search for new physics in final states with jets and missing transverse momentum in $\sqrt{s} = 13$ TeV pp collisions with the α_T variable”, Technical Report CMS-PAS-SUS-15-005, CERN, Geneva, 2015.
- [9] C. G. Lester and D. J. Summers, “Measuring masses of semiinvisibly decaying particles pair produced at hadron colliders”, *Phys. Lett. B* **463** (1999) 99, doi:10.1016/S0370-2693(99)00945-4, arXiv:hep-ph/9906349.
- [10] CMS Collaboration, “Performance of Electron Reconstruction and Selection with the CMS Detector in Proton-Proton Collisions at $s = 8$ TeV”, *JINST* **10** (2015), no. 06, P06005, doi:10.1088/1748-0221/10/06/P06005, arXiv:1502.02701.
- [11] A. L. Read, “Presentation of search results: The CL_s technique”, *J. Phys. G* **28** (2002) 2693, doi:10.1088/0954-3899/28/10/313.
- [12] A. L. Read, “Modified frequentist analysis of search results (The CL_s method)”, *CERN-OPEN* **205** (2000).
- [13] G. Cowan, K. Cranmer, E. Gross, and O. Vitells, “Asymptotic formulae for likelihood-based tests of new physics”, *Eur. Phys. J. C* **71** (2011) 1554, doi:10.1140/epjc/s10052-011-1554-0, arXiv:1007.1727.
- [14] ATLAS and CMS Collaborations, “Procedure for the LHC Higgs boson search combination in summer 2011”, CMS NOTE/ATL-PHYS-PUB ATL-PHYS-PUB-2011-011, CMS-NOTE-2011-005, 2011.

- [15] CMS Collaboration, “Search for top-squark pair production in the single-lepton final state in pp collisions at $\sqrt{s} = 8$ TeV”, *Eur. Phys. J.* **C73** (2013), no. 12, 2677, doi:10.1140/epjc/s10052-013-2677-2, arXiv:1308.1586.

A Detailed Results

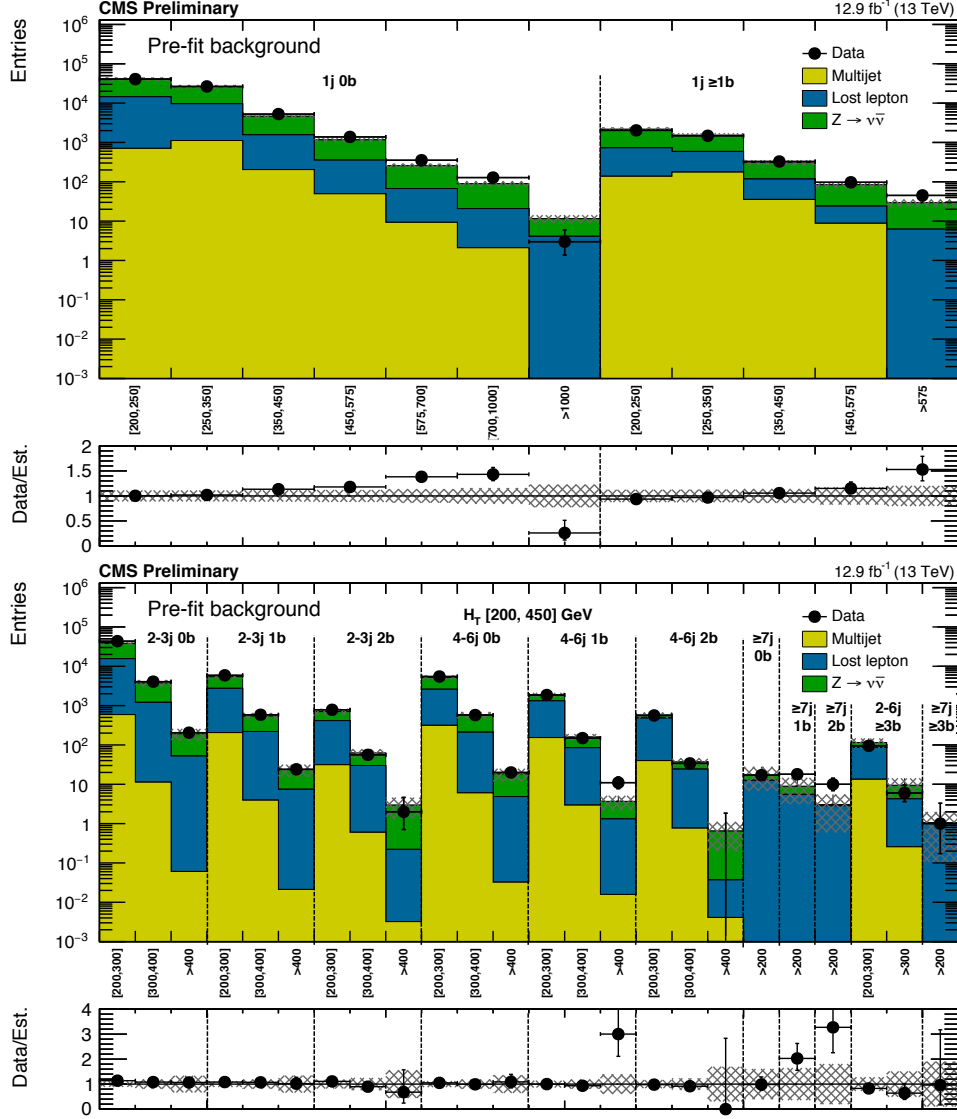


Figure 8: (Above) Comparison of the estimated background and observed data events in each signal bin in the mono-jet region. On the x -axis, the p_T^{jet1} binning is shown (in GeV). Hatched bands represent the full uncertainty on the background estimate. (Below) Same for the very low H_T region. On the x -axis, the M_{T2} binning is shown (in GeV). Bins with no entry for data have an observed count of 0.

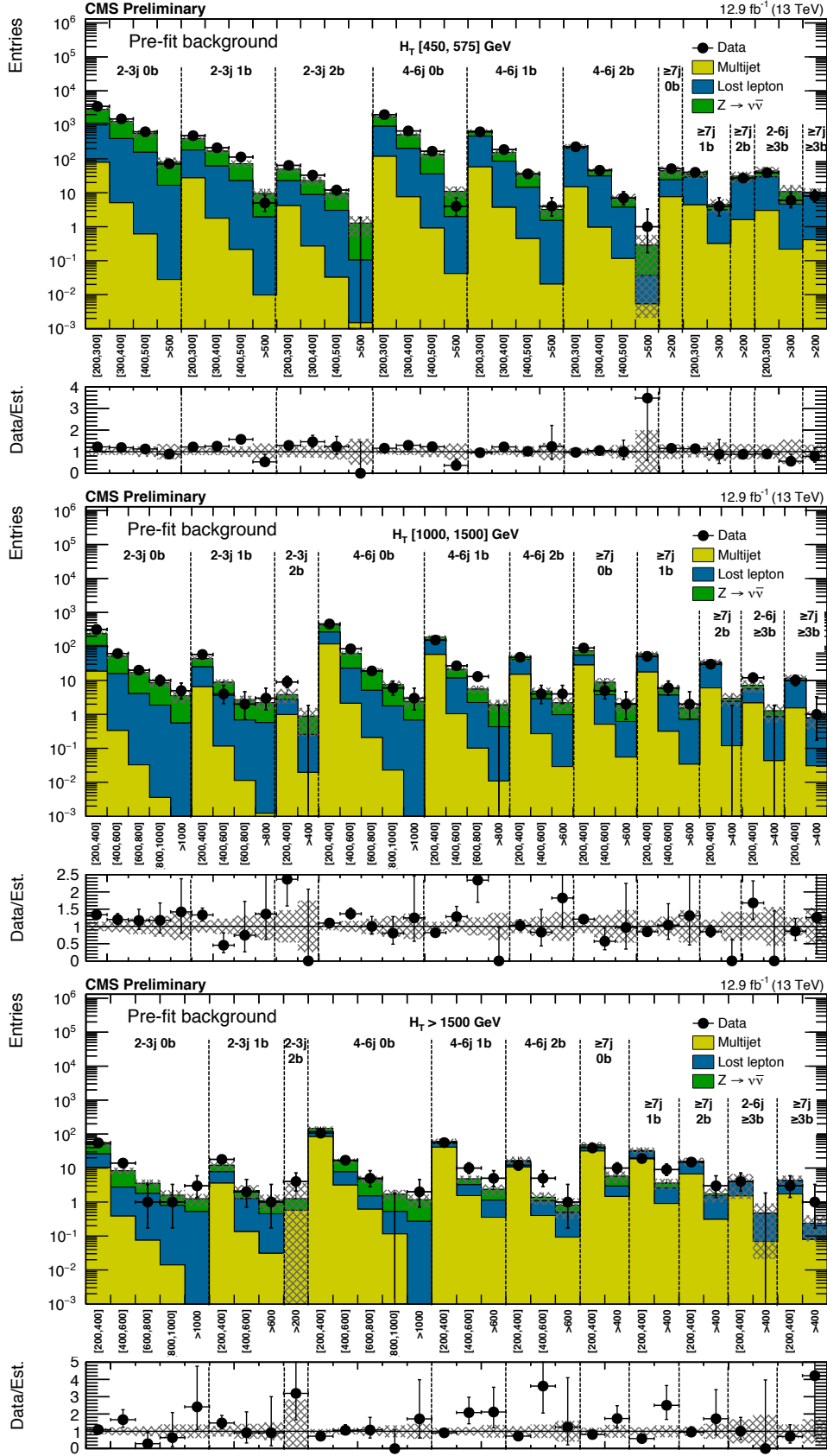


Figure 9: (Top) Comparison of the estimated background and observed data events in each signal bin in the low H_T region. Hatched bands represent the full uncertainty on the background estimate. Same for the high (middle) and extreme (bottom) H_T regions. On the x -axis, the M_{T2} binning is shown (in GeV). Bins with no entry for data have an observed count of 0.

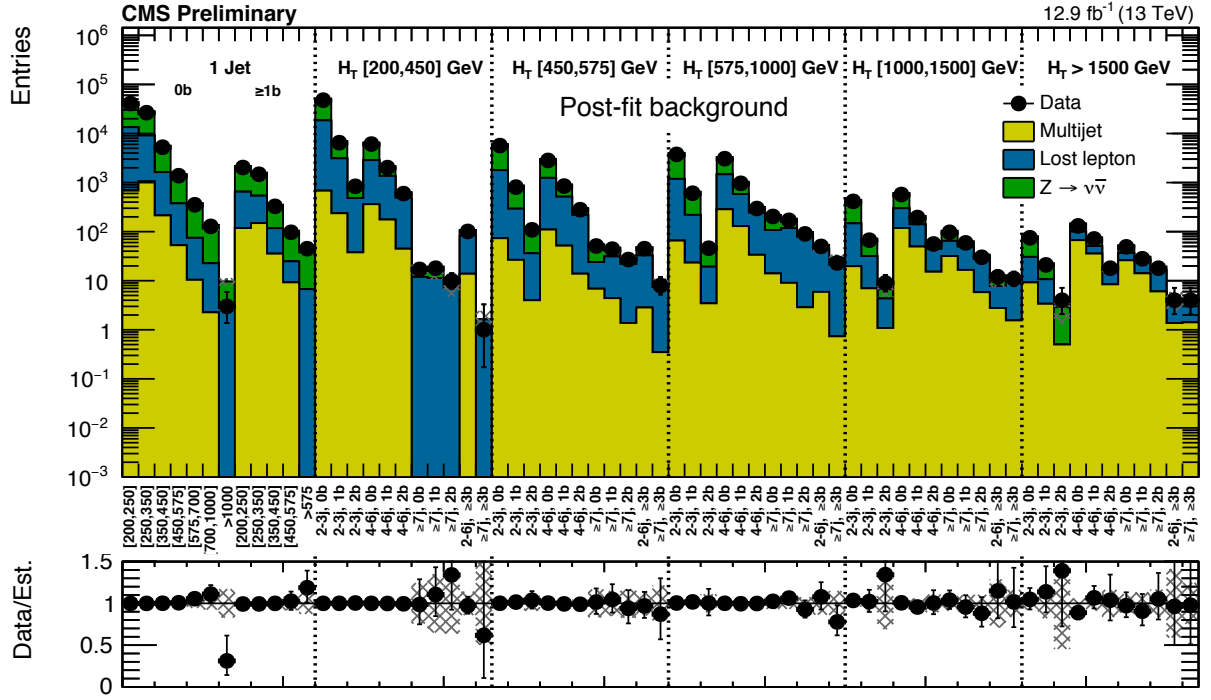


Figure 10: Comparison of post-fit background prediction and observed data events in each topological region. Hatched bands represent the post-fit uncertainty on the background prediction. For the monojet, on the x -axis the $p_T^{\text{jet}1}$ binning is shown (in GeV), whereas for the multijet signal regions, the notations j, b indicate N_j, N_b labeling.

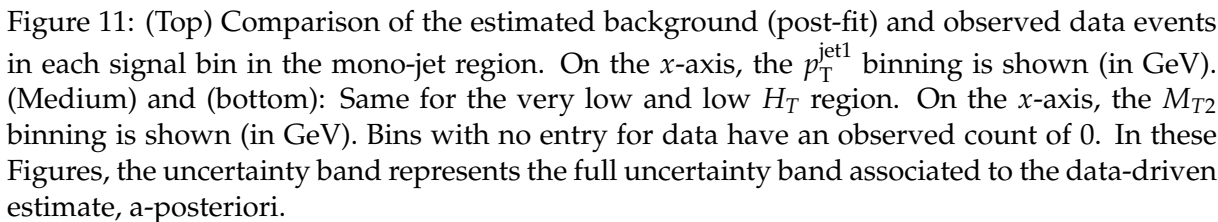


Figure 11: (Top) Comparison of the estimated background (post-fit) and observed data events in each signal bin in the mono-jet region. On the x -axis, the p_T^{jet1} binning is shown (in GeV). (Medium) and (bottom): Same for the very low and low H_T region. On the x -axis, the M_{T2} binning is shown (in GeV). Bins with no entry for data have an observed count of 0. In these Figures, the uncertainty band represents the full uncertainty band associated to the data-driven estimate, a-posteriori.

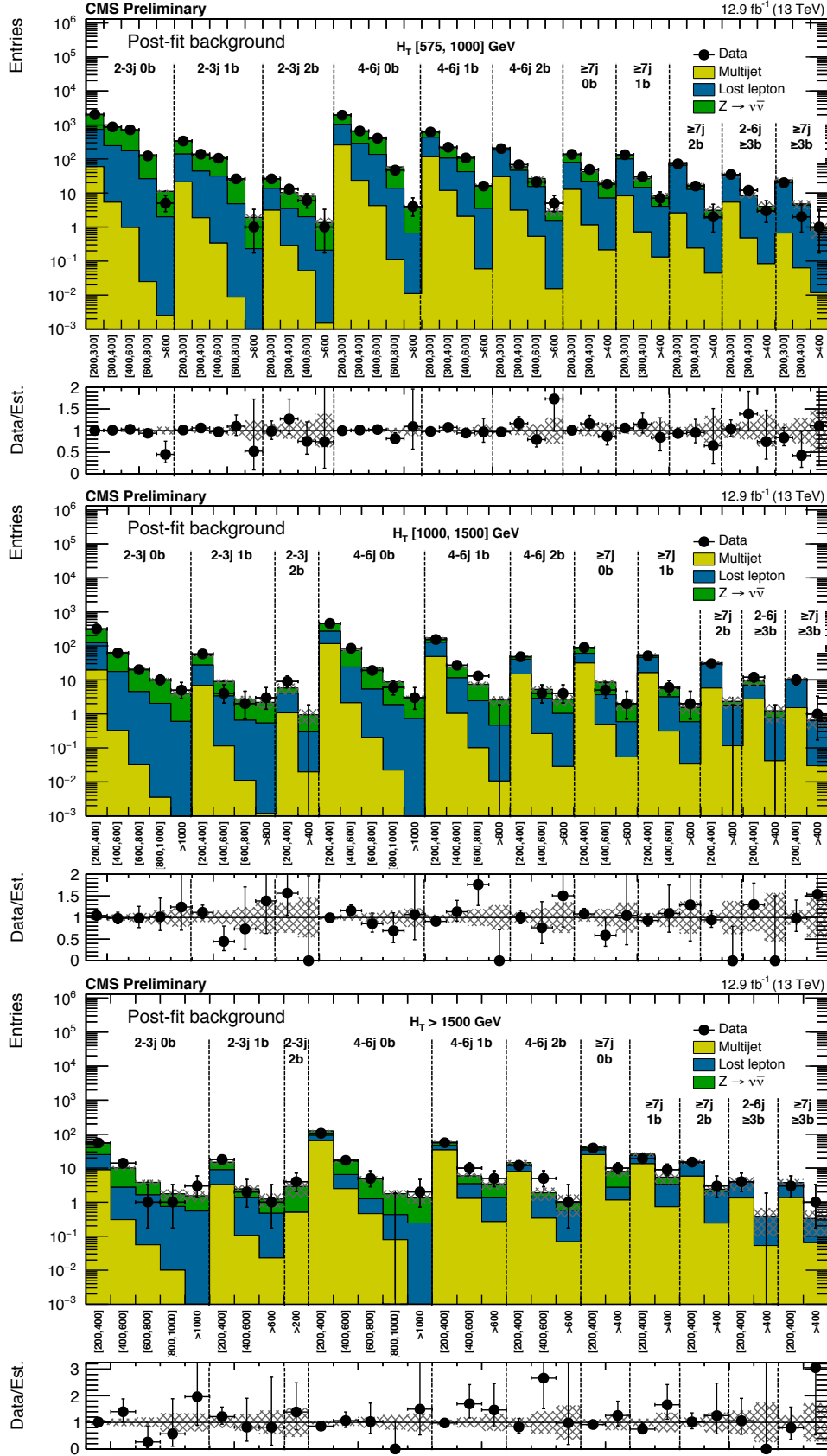


Figure 12: (Top) Comparison of the estimated background (post-fit) and observed data events in each signal bin in the medium H_T region. Same for the high (middle) and extreme (bottom) H_T regions. On the x-axis, the M_{T2} binning is shown (in GeV). Bins with no entry for data have an observed count of 0. In these Figures, the uncertainty band represents the full uncertainty band associated to the data-driven estimate, a-posteriori.

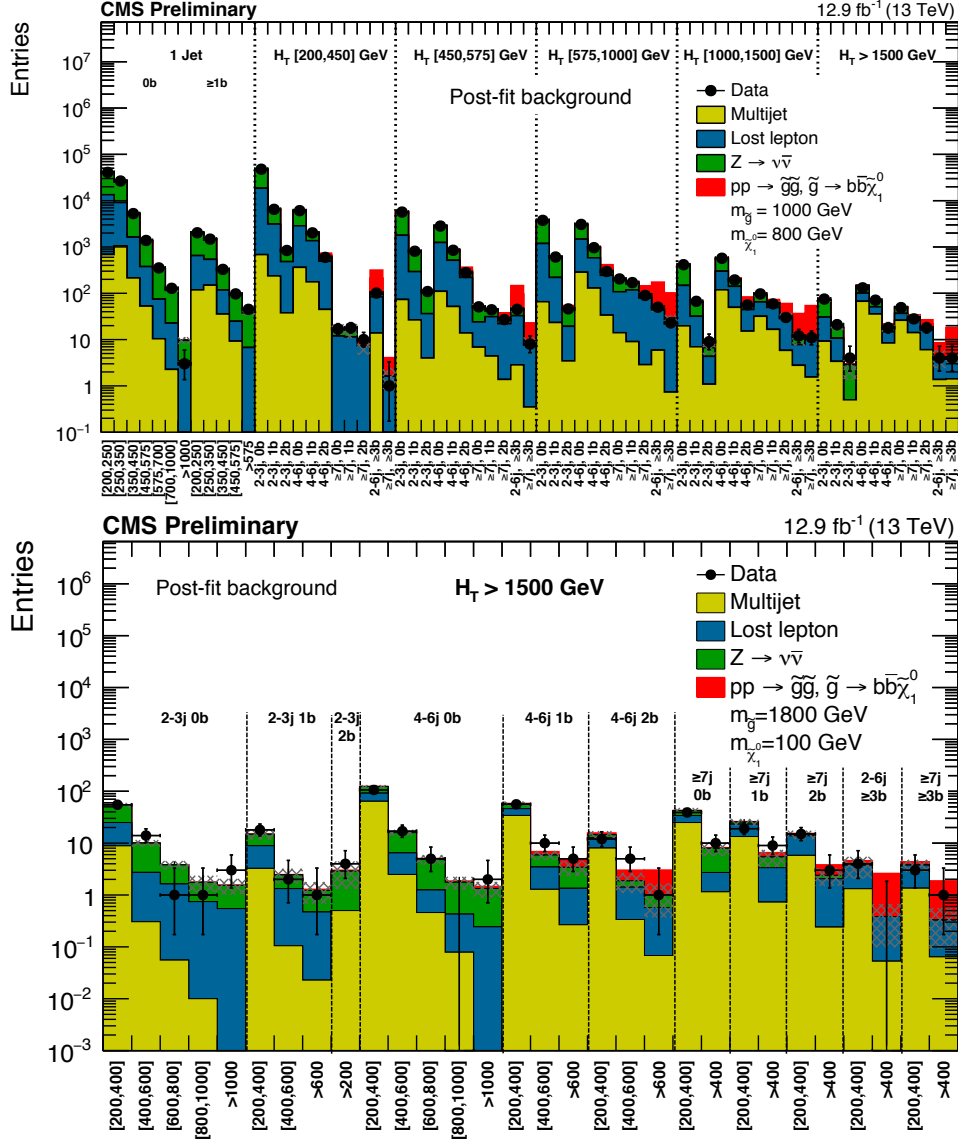


Figure 13: (Above) Expected (post-fit) and observed yields in the analysis binning, for all topological regions with the expected yield for the signal model of gluino mediated bottom-squark production ($m_{\tilde{g}} = 1000$ GeV, $m_{\tilde{\chi}_1^0} = 800$ GeV) stacked on top of the expected background. For the monojet regions, on the x -axis is shown the p_T^{jet1} binning (in GeV). (Below) Same for the extreme H_T region for the same signal with ($m_{\tilde{g}} = 1800$ GeV, $m_{\tilde{\chi}_1^0} = 100$ GeV). In these Figures, the uncertainty band represents the full uncertainty band associated to the data-driven estimate, a-posteriori.

B Aggregated regions

To allow simpler reinterpretations, we also provide our results in “aggregated regions,” made from summing up the event yields and the pre-fit background predictions for individual signal bins in topologically similar regions. The uncertainty in the prediction in each aggregated region is calculated taking into account the same correlation model used in the full analysis. The definitions of these regions are given in Table 3, while Table 4 gives the predicted and observed number of events in each region together with the 95% CL upper limit on the number of signal events.

Table 3: Definitions of aggregate regions. All selections listed for a given region are considered in a logical OR.

Region	N_j	N_b	H_T [GeV]	M_{T2} [GeV]
1j loose	$= 1$	-	> 575	-
	2-3	≤ 2	575-1000	> 600
	2-3	≤ 2	> 1000	> 200
1j medium	$= 1$	$= 0$	> 1000	-
	$= 1$	≥ 1	> 575	-
	2-3	$= 0$	575-1000	> 800
	2-3	1-2	575-1000	> 600
	2-3	0-1	1000-1500	> 800
	2-3	$= 2$	1000-1500	> 400
	2-3	0-1	> 1500	> 400
	2-3	$= 2$	> 1500	> 200
2j medium	2-3	-	> 1000	> 600
	2-3	-	> 1500	> 400
	4-6	-	> 1000	> 800
	4-6	-	> 1500	> 600
2j tight	2-6	0	> 1000	> 1000
	2-6	1-2	> 1000	> 600
	2-6	3	> 1000	> 400
4j medium	≥ 4	-	> 1000	> 600
	≥ 7	-	> 1500	> 400
4j tight	≥ 4	-	> 1500	> 600
	≥ 7	-	> 1500	> 400
7j tight	≥ 7	0-1	> 1000	> 600
	≥ 7	≥ 2	> 1000	> 400
	≥ 7	-	> 1500	> 400
7j verytight	≥ 7	-	> 1000	> 400
2b medium	≥ 2	≥ 2	> 575	> 400
2b tight	≥ 2	≥ 2	> 1000	> 400
2b verytight	≥ 2	≥ 2	> 1500	> 400
3b medium	≥ 2	≥ 3	> 575	> 200
3b tight	≥ 2	≥ 3	> 1000	> 200
3b verytight	≥ 2	≥ 3	> 1000	> 400

If these aggregated regions are used to derive cross section limits on the signals considered in this paper, they typically yield results that are less stringent by a factor of about two compared to the full binned analysis. This is shown in more detail for few signal models in Table 5. The expected upper limit on the signal cross section as obtained from the full analysis is compared

Table 4: Predictions and observations for the aggregated regions defined in Table 3, together with the observed 95% CL limit on the number of signal events contributing to each region (N_{95}^{obs}). An uncertainty of either 15 or 30% in the signal efficiency is assumed for calculating the limits.

Region	Prediction	Observation	$N_{95}^{\text{obs}}, 15\% \text{ unc.}$	$N_{95}^{\text{obs}}, 30\% \text{ unc.}$
1j loose	978^{+91}_{-93}	1274	496	567
1j medium	105^{+13}_{-13}	125	53	58
2j medium	$81.9^{+11.8}_{-11.9}$	97	44	49
2j tight	$25.5^{+4.5}_{-4.0}$	33	21	24
4j medium	$77.8^{+10.8}_{-10.6}$	93	42	47
4j tight	$22.4^{+4.4}_{-4.2}$	36	28	31
7j medium	$60.0^{+13.6}_{-11.6}$	67	34	37
7j tight	$18.7^{+4.5}_{-4.0}$	28	22	25
7j verytight	$11.3^{+3.1}_{-2.9}$	23	23	26
2b medium	$71.7^{+12.2}_{-12.0}$	69	28	30
2b tight	$27.0^{+5.4}_{-4.6}$	30	18	19
2b verytight	$5.9^{+2.6}_{-1.6}$	14	17	19
3b medium	110^{+16}_{-15}	104	31	34
3b tight	$29.8^{+5.7}_{-5.2}$	31	17	19
3b verytight	$2.8^{+1.0}_{-0.9}$	2	4.5	4.5

to the one obtained from the aggregated region that has the best sensitivity to the signal model considered. A 15% uncertainty in the signal selection efficiency is assumed for calculating these limits. The same table also provides the expected signal yields in the given aggregated regions.

Table 5: Expected upper limits on the cross section of several signal models, as determined from the full binned analysis, are compared to the upper limits obtained using only the aggregated region that has the best sensitivity to each considered signal model. A 15% uncertainty in the signal selection efficiency is assumed for calculating these limits. The signal yields expected for an integrated luminosity of 12.9 fb^{-1} are also shown.

Signal	Expected limit [fb] (full analysis)	Best aggregated region	Signal yield (best aggregated region)	Expected limit [fb] (best aggregated region)
$pp \rightarrow \tilde{g}\tilde{g}, \tilde{g} \rightarrow b\bar{b}\tilde{\chi}_1^0$ ($m_{\tilde{g}} = 1700 \text{ GeV}, m_{\tilde{\chi}_1^0} = 0 \text{ GeV}$)	1.80	2b tight	18.8	3.84
$pp \rightarrow \tilde{g}\tilde{g}, \tilde{g} \rightarrow b\bar{b}\tilde{\chi}_1^0$ ($m_{\tilde{g}} = 1000 \text{ GeV}, m_{\tilde{\chi}_1^0} = 950 \text{ GeV}$)	234	2b tight	10.0	498
$pp \rightarrow \tilde{g}\tilde{g}, \tilde{g} \rightarrow q\bar{q}\tilde{\chi}_1^0$ ($m_{\tilde{g}} = 1600 \text{ GeV}, m_{\tilde{\chi}_1^0} = 0 \text{ GeV}$)	4.05	4j tight	27.4	4.51
$pp \rightarrow \tilde{g}\tilde{g}, \tilde{g} \rightarrow q\bar{q}\tilde{\chi}_1^0$ ($m_{\tilde{g}} = 1000 \text{ GeV}, m_{\tilde{\chi}_1^0} = 850 \text{ GeV}$)	244	7j medium	34.1	281
$pp \rightarrow \tilde{g}\tilde{g}, \tilde{g} \rightarrow t\bar{t}\tilde{\chi}_1^0$ ($m_{\tilde{g}} = 1500 \text{ GeV}, m_{\tilde{\chi}_1^0} = 0 \text{ GeV}$)	3.69	2b verytight	13.5	10.3
$pp \rightarrow \tilde{g}\tilde{g}, \tilde{g} \rightarrow t\bar{t}\tilde{\chi}_1^0$ ($m_{\tilde{g}} = 900 \text{ GeV}, m_{\tilde{\chi}_1^0} = 600 \text{ GeV}$)	312	3b tight	18.6	595
$pp \rightarrow \tilde{t}\tilde{t}, \tilde{t} \rightarrow t\tilde{\chi}_1^0$ ($m_{\tilde{t}} = 750 \text{ GeV}, m_{\tilde{\chi}_1^0} = 0 \text{ GeV}$)	18.6	2b medium	36.2	34.9
$pp \rightarrow \tilde{t}\tilde{t}, \tilde{t} \rightarrow t\tilde{\chi}_1^0$ ($m_{\tilde{t}} = 600 \text{ GeV}, m_{\tilde{\chi}_1^0} = 250 \text{ GeV}$)	79.5	2b medium	20.2	254
$pp \rightarrow \tilde{t}\tilde{t}, \tilde{t} \rightarrow t\tilde{\chi}_1^0$ ($m_{\tilde{t}} = 250 \text{ GeV}, m_{\tilde{\chi}_1^0} = 150 \text{ GeV}$)	9236	4j medium	15.2	42345
$pp \rightarrow \tilde{b}\tilde{b}, \tilde{b} \rightarrow b\tilde{\chi}_1^0$ ($m_{\tilde{b}} = 800 \text{ GeV}, m_{\tilde{\chi}_1^0} = 0 \text{ GeV}$)	11.5	2j tight	13.4	31.5
$pp \rightarrow \tilde{b}\tilde{b}, \tilde{b} \rightarrow b\tilde{\chi}_1^0$ ($m_{\tilde{b}} = 500 \text{ GeV}, m_{\tilde{\chi}_1^0} = 350 \text{ GeV}$)	362	2b medium	26.5	573
$pp \rightarrow \tilde{q}\tilde{q}, \tilde{q} \rightarrow q\tilde{\chi}_1^0, \tilde{q}_L + \tilde{q}_R (\tilde{u}, \tilde{d}, \tilde{s}, \tilde{c})$ ($m_{\tilde{q}} = 1400 \text{ GeV}, m_{\tilde{\chi}_1^0} = 0 \text{ GeV}$)	3.41	2j tight	9.48	5.96
$pp \rightarrow \tilde{q}\tilde{q}, \tilde{q} \rightarrow q\tilde{\chi}_1^0, \tilde{q}_L + \tilde{q}_R (\tilde{u}, \tilde{d}, \tilde{s}, \tilde{c})$ ($m_{\tilde{q}} = 600 \text{ GeV}, m_{\tilde{\chi}_1^0} = 300 \text{ GeV}$)	208	7j tight	26.5	753